Title: N-dihydrogalactochitosan reduces mortality in a lethal mouse model of SARS-CoV-2

Single Sentence Summary: The immunoadjuvant N-dihydrogalactochitosan diminishes SARS-CoV-2 disease in humanized ACE2 mice representing a new countermeasure against COVID-19.

Authors: Christopher M. Weiss[1,4], Hongwei Liu[1], Erin E. Ball[1], Samuel Lam[2], Tomas Hode[2], M. Kevin Keel[1], Richard M. Levenson[3], and Lark L. Coffey[1*]

[1] Department of Pathology, Microbiology & Immunology, University of California, Davis, CA

[2] Immunophotonics, Inc., Saint Louis, MO

[3] Department of Pathology and Laboratory Medicine, UC Davis Health, Sacramento, CA

[4] Current address: Meissa Vaccines, Inc., Redwood City, CA

*Corresponding Author

lcoffey@ucdavis.edu

ORCID iD:

Christopher Weiss 0000-0003-4704-9533

Hongwei Liu 0000-0002-8342-2545

Erin Ball 0000-0002-8464-6612

Richard Levenson 0000-0002-0112-6823

Lark Coffey 0000-0002-0718-5146

ABSTRACT

The rapid emergence and global dissemination of SARS-CoV-2 that causes COVID-19 continues to cause an unprecedented global health burden resulting in more than 4 million deaths in the 20 months since the virus was discovered. While multiple vaccine countermeasures have been approved for emergency use, additional treatments are still needed due to sluggish vaccine rollout and vaccine hesitancy. Immunoadjuvant compounds delivered intranasally can guide non-specific innate immune responses during the critical early stages of viral replication, reducing morbidity and mortality. N-dihydro**g**alacto**c**hitosan (GC) is a novel mucoadhesive immunostimulatory polymer of β-0-4-linked N-acetylglucosamine that is solubilized by the conjugation of galactose glycans. We tested GC as a potential countermeasure for COVID-19. GC administered intranasally before and after SARS-CoV-2 exposure diminished morbidity and mortality in humanized ACE2 receptor expressing mice by up to 75% and reduced infectious virus levels in the upper airway and lungs. Our findings demonstrate a new application for soluble immunoadjuvants like GC for preventing severe disease associated with SARS-CoV-2.

INTRODUCTION

Severe acute respiratory syndrome-like coronavirus 2 (SARS-CoV-2) that was first identified from a cluster of viral pneumonia cases in Wuhan, China in December 2019 *(1)* has caused more than 202 million cases and nearly 4.3 million deaths globally as of August 9, 2021. Clinical manifestations of 2019 novel coronavirus disease (COVID-19) caused by SARS-CoV-2 typically include fever, non-productive cough, and mild to moderate dyspnea, with severe cases developing pneumonia and acute respiratory distress syndrome *(1–3)*. SARS-CoV-2 morbidity and mortality increase with age and systemic proinflammatory and cardiovascular co-morbidities *(1, 2, 4)*. Recovered patients may also exhibit long-duration symptoms including disruption to sensations of taste and smell, and cognitive impairment (colloquially referred to as “brain fog”) resulting from neurological involvement *(5, 6)*.

Like SARS-CoV, SARS-CoV-2 uses the angiotensin converting enzyme 2 (ACE2) for cell entry *(7, 8)*. Small animals including mice, hamsters, and ferrets, have been fundamental in defining SARS-CoV-2 pathogenesis and developing medical countermeasures *(9, 10)*. Transgenic mice expressing the human ACE2 (hACE2) gene from the human cytokeratin 18 (K18) promoter have served as an especially useful model of severe disease due to well characterized genetics and ease of use *(11–13)*. Intranasal inoculation of K18-hACE2 mice (hereafter termed hACE2) with SARS-CoV-2 results in a high viral burden in the lungs, which diminishes past day 7, and elevated viral loads detectible in the brain at day 7 *(12)*.

SARS-CoV-2, which can be transmitted in small-droplet aerosols from person to person, can take up to 14 days to produce symptoms *(14)*. Public health countermeasures have evolved as additional treatments and information regarding transmission risks for COVID-19 have become available. In addition to face coverings and physical distancing, multiple vaccine candidates have now received emergency use authorization by the United States Food and Drug Administration (FDA) *(15)*. While ‘herd immunity’ through vaccination remains the target, it is estimated that 70-90% of the global population must be immune in order to interrupt

transmission *(16)*. This target becomes even more challenging with high levels of vaccine skepticism, slow production, inequitable distribution, and the rise of variants of concern capable of more efficient transmission or vaccine escape. Pre- and post-exposure countermeasures can help fill the vaccine gap by reducing COVID-19 morbidity and mortality in unprotected communities and thus reduce the global burden of the pandemic. The nucleoside analog remdesivir *(17)* is the only current FDA-approved therapeutic and was authorized based on its ability to shorten recovery time in COVID-19 patients *(18)*, but it is not ideal for clinical use due to its only moderate clinical efficacy *(19)*, as well as its requirement for intravenous administration. As of October 2020, there were nearly 400 active trials of therapeutic agents with more than 10 drugs or biological products holding emergency use authorization, mostly indicated for patients with severe COVID-19 *(20)*. Despite these advances, there are presently no drugs available for high-risk exposure use to protect against SARS-CoV-2. To circumvent this gap, we repurposed a therapy used for cancer and as a vaccine adjuvant with a goal of mitigating COVID-19 disease.

The parent compound of GC, chitosan, is a linear biological polysaccharide polymer of β-0-4-linked N-acetylglucosamine and is produced from alkaline treatment of the chitin exoskeleton of crustaceans. Chitosan is approved by the FDA for tissue engineering and drug delivery. Chitosan shows broad acting antiviral *(21)* and immunoadjuvant properties *(22, 23)* including interferon (IFN) induction *(24, 25)* that is critical for viral control *(26–28)*, and has been successfully tested as an antiviral therapy for respiratory viruses *(29–31)*. Modification of chitosan by attaching galactose molecules to the free amino acids on the polysaccharide backbone produces N-dihydro**g**alacto**c**hitosan (GC) *(32, 33)*. GC was initially designed to further improve immune stimulating function of the molecular backbone by adding glycan moieties, which can bind to C-type lectin receptors on antigen presenting cells *(34)* and lead to a downstream immune responses while retaining the mucoadhesive properties of the parent molecule *(35)*. Furthermore, GC has improved solubility at physiological pH ranges compared to

its parent molecule, and hence is more suitable as an injectable agent. With these modifications, GC has been developed for use in human interventional immuno-oncology to stimulate systemic anti-tumor immunity *(36)*. GC recruits granulocytes at the injection site *(37)* and stimulates activation of dendritic cells and macrophages through upregulation of co-stimulatory molecules CD40, CD86, and MHCII *in vitro* and *in vivo (38, 39)* . Macrophages also show increased nitric oxide production and phagocytic abilities *(38)*. Single-cell RNA sequencing indicates enrichment of type I IFN signaling in multiple innate immune cells, including monocytes, M1 macrophages, and neutrophils in tumors following GC administration *(40)*. Broad-acting non-toxic immunoadjuvants like GC that upregulate innate immune responses and recruit cellular responses to the exposure site represent a novel approach against SARS-CoV-2. Furthermore, non-specific immunoadjuvants such as GC could offer a benefit over more narrowly targeted antivirals by providing protection against a range of pathogens, potentially including future agents not yet affecting public health.

In the present study, we explored the use of GC for prophylaxis against SARS-CoV-2 infection applied pre- and post-exposure to lethal dosages of the virus in transgenic hACE2 mice. To simulate the use of solubilized GC as a nasal spray, we applied the compound intranasally twice before exposure and once following exposure of mice to a human isolate of SARS-CoV-2. Our data demonstrate a strong protective effect from GC in preventing mortality in this lethal model of disease. Pre- and post-exposure countermeasures can help fill the vaccine gap by reducing COVID-19 morbidity and mortality in unprotected communities and reduce the global burden of the pandemic.

RESULTS

N-dihydrogalactochitosan reduces SARS-CoV-2-associated mortality in hACE2 transgenic mice.

To determine the antiviral efficacy of N-dihydro**g**alacto**c**hitosan (GC) against SARS-CoV-2, 6-week-old hACE2 [B6.Cg-Tg(K18-ACE2)2Prlmn/J] mice were treated intranasally (i.n.) with 0.75% of GC in neutral buffered saline 3 and 1 days prior to virus exposure and 1 day post exposure (**Fig. 1a**). Inhaled GC was well tolerated in mice, and no adverse events were noted during or after treatment. Mice were challenged i.n. 1 day prior to the final GC treatment with 10^3 or 10^4 plaque forming units (PFU) of SARS-CoV-2, a route and dose intended to produce high lethality in this model. Inocula were back-titrated to verify the administered dose. Tracheal swabs were collected for the first 3 days post challenge and animals were monitored daily until day 14 for weight loss and health status.

Weight remained stable for the first 3 days in all groups and infected controls rapidly declined starting at day 4 in 10^4 PFU and day 5 in 10^3 PFU groups (**Fig. 1b**). Half of mice experienced no weight loss throughout the duration of the study (**Supplementary Fig. 1**); conversely, their growth outpaced mock-infected counterparts treated with saline alone (p<0.0001). This effect was not limited to one biological sex and did not correlate with mouse starting weight at the time of study initiation. Additional mice lost weight starting at day 4 but failed to reach euthanasia criteria (loss of 20% of initial body weight) and recovered to starting weight by day 14 post-challenge. Relative to the 10^4 group, mice challenged with 10^3 PFU SARS-CoV-2 exhibited delayed or transient weight loss, with 1 mouse experiencing no weight loss over the duration of the study. At the higher challenge dose of 10^4 PFU, GC significantly reduced weight loss versus delivery vehicle treated controls (p<0.0001). At the lower 10^3 PFU challenge dose, GC trended toward protection from weight loss, which was confounded by non-uniform disease in delivery vehicle treated controls (p=0.11). Mice treated with delivery vehicle and challenged with 10^3 or 10^4 PFU had a median survival time of 7±3.3 and 6.5±0.9 days, respectively (**Fig. 1c**). At the lower challenge dose of 10^3 PFU, GC had an efficacy of 37.5% protection from mortality (p=0.05) (**Fig. 1d**). At the higher challenge dose of 10^4 PFU, GC

reduced SARS-CoV-2 mortality by 75% (p<0.0001). Together, these results demonstrate the potent efficacy of GC in preventing fatal SARS-CoV-2 disease in transgenic mice.

N-dihydrogalactochitosan reduces SARS-CoV-2 viral levels in the upper respiratory tract. We next sought to determine whether GC reduced viral levels in addition to protecting mice from mortality. Infectious SARS-CoV-2 levels were assessed longitudinally in mice by swabbing throats from day 1 to 3 post-challenge (**Fig. 2a**). SARS-CoV-2 was detectible in the trachea of infected animals at day 1 post challenge and most animals had no detectible virus by day 3. Virus levels were elevated in mice inoculated with 10^4 PFU versus 10^3 PFU at 1 day post challenge (p=0.05), but differences between challenge doses were not detected after day 2 (p>0.99). GC significantly reduced virus levels in the trachea at day 1 and day 2 post challenge with 10^4 PFU (p=0.0005 and p=0.02, respectively). A similar effect was not observed in mice receiving the lower inoculum of 10^3 PFU. All delivery vehicle-treated mice had detectible virus in swabs following infection, while 29.2% (7/24) of mice had no infectious virus isolated between days 1 and 3. Positive virus detection in tracheal swabs was not correlated with lethal disease in mice (p=0.62, Fisher's exact test). Cumulative virus levels in tracheal swabs were calculated as area under the curve for individual animals (**Fig. 2b**). GC significantly reduced the total virus levels in mice challenged with 10^4 PFU from a geometric mean of 225 to 5.6 PFU collected in swabs (p<0.0001) and trended toward a reduction in animals challenged with 10^3 PFU from 138 to 15 PFU collected in swabs (p=0.08).

As individual animals met humane experimental endpoints, mice were euthanized between days 5 and 7. Infectious virus levels were measured in the lungs (**Fig. 2c**) and brain (**Fig. 2d**) at the time of death. The geometric mean lung viral titers ranged from 89 to 1209 PFU/mg in delivery vehicle-treated control animals. Similarly, GC-treated mice had geometric mean lung titers ranging from 6 to 1004 PFU/mg. GC treatment trended toward a reduction in

lung virus levels (F=2.431, p=0.06, two-way ANOVA) with cumulative effects in animals challenged with 10^3 PFU driving the main treatment effect (p=0.06).

Comparatively high viral titers were observed in the brain at the time of death, consistent with previous descriptions in this model *(12)*. Virus was detectible in the brain in all but 2 infected animals at the time of death, indicating neuroinvasion as a likely cause of morbidity. Delivery vehicle-treated control animals had geometric mean brain titers ranging from 13,695 to 21,4045 PFU/mg. Geometric mean brain titers in GC-treated animals ranged from 1,351 to 24,299 PFU/mg. No significant trends in brain virus levels were observed between treatments (F=0.8134, p=0.52, two-way ANOVA). No infectious virus was detectible in the lungs or brains of animals euthanized at day 14 post challenge.

N-dihydrogalactochitosan reduces the severity of histopathologic lesions associated with SARS-CoV-2 infection in lungs.

Intranasal inoculation of hACE2 transgenic mice with PBS followed by mock inoculation resulted in normal lung architecture in most mice, although several animals exhibited mild alveolar septal inflammation, likely associated with i.n. administration **(Fig. 3a)**. By contrast, mice inoculated with 10^3 or 10^4 PFU SARS-CoV-2 (**Fig. 3c**, representative 10^3 image shown) exhibited extensive lymphohistiocytic interstitial pneumonia with a peribronchiolar and perivascular distribution and scattered multinucleated syncytial cells. Bronchiolitis, bronchiolar epithelial and alveolar septal necrosis, hemorrhage, fibrin, edema, and vascular endothelial inflammation were also occasionally noted. SARS-CoV-2-infected mice treated with GC showed lesser histopathologic lesions in the lung (**Fig. 3b**) compared to animals that did not receive GC, and inflammation was focally distributed instead of widespread. To quantify histopathologic changes, lung lesion severity (**Fig. 3d**) was scored using specific criteria (**Supplementary Table 1**) and the total area of the lung that was affected was estimated using image analysis software (**Fig. 3e**). GC treatment significantly reduced the mean severity score for animals dosed with 10^4 PFU SARS-CoV-2 from 4.6 to 2.5 (ANOVA, $p < 0.0001$). Mean scores for mice

treated with GC and 10^3 PFU of SARS-CoV-2 trended towards being lower than for mice who did not receive GC but were not significantly different ($p > 0.05$). The percent of lung affected in mice that received the 10^4 SARS-CoV-2 dose was also significantly reduced from a mean of 33% to 13% ($p < 0.0001$); differences at the 10^3 dose were not significant.

A subset of GC-treated and untreated mice exhibited mild rhinitis, characterized by mucus, sloughed cells, necrotic debris, and scattered neutrophils in the nasal cavity. One GC-treated mouse (**Supplementary Fig. 2a**) and 3 mock-inoculated mice exhibited pulmonary foreign-material reactions, with necrosuppurative bronchiolitis and multiple foci of neutrophils, macrophages, and multinucleated giant cells surrounding intracellular and extracellular brightly eosinophilic foreign material. Consistent with high viral titers in the brain, some GC-treated and untreated mice exhibited mild to moderate lymphocytic meningitis with perivascular cuffing and occasional extension of lymphocytes into the adjacent neuropil (**Supplementary Fig. 2b,c**). Together, these data show that GC reduces SARS-CoV-2-induced disease in the lung of hACE2 mice, although only significantly in mice administered the higher 10^4 PFU dose of SARS-CoV-2. The pulmonary foreign material reactions and alveolar inflammation in both GC- and mock-treated mice may stem from the volume or frequency of i.n. treatment; future studies using GC could modify both parameters as a means to reduce these lesions.

Mice treated with N-dihydrogalactochitosan produce neutralizing antibodies after SARS-CoV-2 exposure.

Finally, we sought to determine whether mice surviving SARS-CoV-2 challenge produced a humoral immune response that might protect them from future challenge. Serum from blood collected at day 14 post inoculation was assessed for neutralizing antibody against the challenge strain of SARS-CoV-2 by plaque reduction neutralization test (PRNT) at the 80% neutralization threshold (**Fig. 4**). All infected mice surviving viral challenge generated neutralizing antibodies. Mice in the GC group challenged with 10^3 or 10^4 PFU generated geometric mean neutralizing titers of 1:676 and 1:861, respectively. In comparison, PBS-

administered mice that received a challenge dose of 10^3 PFU had a mean neutralizing titer of 1:1448. Neutralizing antibody titers were not different across treatments ($p>0.9999$) or virus dose, although PBS-administered mice challenged with 10^4 PFU SARS-CoV-2 were unavailable for comparison due to uniform lethality. These data confirm that surviving mice were productively infected and indicate that animals were able to develop adaptive immune responses that could potentially protect against reinfection.

DISCUSSION

Intranasal administration of GC to prevent or treat SARS-CoV-2 represents a novel application of this potent immunostimulatory compound. In the present study, GC was well-tolerated and prevented lethal disease in up to 75% of treated humanized mice, while all mice not receiving GC but challenged with the 10^4 PFU SARS-CoV-2 had to be euthanized. All surviving animals had neutralizing antibodies detectable at 14 days post inoculation. Similar SARS-CoV-2 antibody titers were detected in GC-treated and untreated animals. Mice that received GC treatment also displayed lower levels of infectious SARS-CoV-2 in tracheal swabs collected 1 to 2 days post inoculation and had less severe lesions in lungs. Reducing virus levels in the upper airway has gained particular significance as recent vaccine breakthrough cases with variants of concern demonstrate SARS-CoV-2 shedding at similar levels to unvaccinated individuals, which is a key determinant of transmission potential *(41)*. Our findings demonstrate a reduction in viral burden and virus-induced disease along with a resultant increase in survival due to GC treatment.

GC is a polymeric mixture containing strands of varying lengths of selectively galactose-conjugated and partially deacetylated β-0-4-linked N-acetylglucosamine molecules with a specific range of molecular weights *(32, 33, 36, 37)*. Synthesized and purified under Good Manufacturing Practice (GMP) conditions, N-dihydrogalactochitosan is a well-characterized variant of GC. Characterization and quality control testing ruled out contamination from

endotoxins, heavy metals, and other impurities, which eliminates a major confounding factor in the research of these naturally derived molecules, and chitosan in particular *(42)*. Water solubility, immunological properties, biocompatibility, and a favorable toxicity profile are key features of GC. The unconjugated base polymer, chitin, is a primary structural component of cell walls for organisms ranging from fungi to arthropods *(21)*. Chitosan, a derivative of chitin, is deacetylated through alkaline treatment and is marketed as a nutritional supplement *(43)* and used as a biopolymer *(44)*. Unmodified chitosan has been used successfully to treat influenza A virus infection in mice *(29)*, demonstrating a potential application as a non-specific antiviral compound for respiratory virus infection. However, unmodified chitosan has low solubility in neutral buffered aqueous solution and requires acidic formulation; poor characterization, purification and lack of controlled synthetic process leads to poor reproducibility and unpredictable outcomes *(42)*. GC circumvents these limitations through a controlled and reproducible process of synthetically attaching galactose to the free-amino groups of the chitosan base, improving solubility (and thus bioavailability) while maintaining a physiological pH. GC has been previously used as a combination anti-tumor therapy due to its immunoadjuvant properties *(38, 40)*, but its utility as a broad-acting antiviral compound has not previously been investigated.

Immunoadjuvants stimulate non-specific innate immune responses through various mechanisms. Some use pattern-recognition receptors, including the Toll-like receptor (TLR) family of antigen detection complexes. While the mechanism of SARS-CoV-2 protection has not been determined for GC, chitosan, and similar polymers of N-acetylglucosamine, interact with TLR2, which serves as a rationale for inclusion of chitosan as a vaccine adjuvant. TLR2 signals through myeloid differentiation factor 88 (MyD88) to stimulate the nuclear factor kappa B (NF-κB) pathway and downstream inflammatory and anti-microbial cytokine responses *(45, 46)*. TLR engagement of the canonical NF-κB pathway up-regulates both tumor necrosis factor alpha (TNF-α) and interleukin-6 (IL-6), two potent pro-inflammatory effectors. IL-6, which is necessary

for antiviral immunity against other virus families, has been identified as a target of dysregulation associated with hyperinflammatory responses in the lungs during SARS-family coronavirus infections. SARS-CoV-1 nucleocapsid protein can stimulate NF-κB activation and IL-6 production independent of infection *(47)*. Prolonged high levels of IL-6 are correlated with severe COVID-19 outcomes in humans, and a similar association has been found in ferrets infected with SARS-CoV-2 *(48)*. The timing of IL-6 production may play a critical role in determining whether viral clearance is achieved or alternatively, hyperinflammatory responses result. Early, but not late, induction of IL-6 during respiratory syncytial virus (RSV), influenza A, and rhinovirus infection promote viral clearance and limit prolonged inflammation by establishing regulatory T cell populations that limit virus spread *(49)*. Similarly, timed induction of pro-inflammatory responses by GC treatment pre- and post-infection may promote viral clearance before virus-mediated dysregulation of this pathway can occur. As such, future studies should explore the timing of GC treatment and regulation of IL-6 and associated pro-inflammatory pathways.

The data in this study demonstrate that treatment with GC induces robust neutralizing antibody responses by day 14, after a reduction in infectious SARS-CoV-2 in tracheal swabs by day 3. These data suggest GC functions as an immunoadjuvant that can modulate innate immune responses after SARS-CoV-2 infection, leading to stimulation of robust antiviral adaptive immunity. Experimental evidence from cell culture and animal models support at least three mechanisms by which complex carbohydrates such as GC could stimulate the innate and adaptive immune systems *(50–53)*. First, GC recognition by sensors on macrophages and dendritic cells (DC) can stimulate innate immune defenses *(54–56)*. While immune receptors for GC have not been identified, chitosan binding to C-type lectin receptors such as dectin-1 can initiate innate immune signaling *(57, 58)*. Second, GC-mediated antigen uptake *(59)* and antigen presentation by DCs could lead to CD4 and CD8 T cell responses *(37, 38)*. Studies in mice show GC induces type 1 IFN *(40)*, leading to enhanced DC activation and robust CD4 T helper

cells *(51)*. Notably, DNA sensor activation is mediated via cellular DNA release by chitosan. Third, physical antigen sequestration and slow antigen release within draining lymph nodes facilitated by GC could potentially prolong germinal center reactions, thereby enhancing humoral immunity by fostering affinity maturation of B cells *(60, 61)*. Thus, GC may have potential as a dual-purpose preventative and therapeutic with immunostimulatory properties. Future studies are needed to investigate the impact of GC on SARS-CoV-2-specific immune responses.

In addition to the immunoadjuvant properties of GC, direct interactions between GC and SARS-CoV-2 in the nasal cavity may contribute to the protection we observed in mice. As the nasopharyngeal and oral cavity are often the primary entry sites of SARS-CoV-2 and other respiratory viruses, interventions or medications at these locations could provide an important boost in the first line of defense. The reduction in SARS-CoV-2 levels in GC treated mice in the first 2 days post-challenge suggests that GC has early effects that hamper the initial phase of viral infection, especially given that serum neutralizing antibodies are not detectable before about 7 days. In addition to possible innate immune stimulation, aqueous GC is viscous and may remain in the airway after intranasal administration. GC present at the time of infection may act as a physical barrier or directly inactivate SARS-CoV-2 before it can initiate infection. Additional studies of GC bioavailability and detailed studies of GC-virus interactions including to establish whether GC blocks virus entry and/or replication are needed to establish mechanisms of protection; these experiments could also clarify why greater protection from lethal disease was observed after challenge with the higher SARS-CoV-2 dose in these studies.

In summary, we show here that GC treatment of humanized mice pre- and post-infection with SARS-CoV-2 reduces lethal disease, virus levels in the upper respiratory tract, and significant lesions in the lungs. These data suggest a possible role of GC as a SARS-CoV-2 countermeasure. Additional pre-clinical studies could focus on the mechanism of protection, including further assessment of the antiviral and immunomodulatory effects of GC. Future

studies should also identify the GC dose and schedule that confer the greatest benefit in reducing disease while minimizing foreign-material reactions as detected in the lungs of several of the mice in this study, as well as to determine whether GC shows both prophylactic and therapeutic benefits.

METHODS

Ethics Statement: All mouse work was conducted on protocol #21868 approved by the institutional animal care and use committee (IACUC) at the University of California, Davis. Infectious virus was handled in certified animal biosafety level 3 laboratory (ABSL-3) spaces in compliance with approved institutional biological use authorization #R2813. The University of California, Davis, is accredited by the Association for Assessment and Accreditation of Laboratory Animal Care (AAALAC). All mouse work adhered to the NIH Guide for the Care and Use of laboratory Animals.

Mice: Equal numbers of male and female transgenic mice expressing the human ACE2 receptor on a K18 transgene in a C57Bl/6J background (B6.Cg-Tg(K18-ACE2)2Prlmn/J, referenced as 'hACE2') were purchased at 5 weeks of age from Jackson Laboratories (Sacramento, CA). Mice were co-housed by sex in ABSL-3 conditions with 4 animals per cage and acclimated for up to 6 days at 22-25°C and a 12:12 hour light: dark cycle. Rodent chow with 18% protein content and sterile bottled water was provided *ad libitum* for the duration of the experiment.

Virus: SARS-CoV-2/human/USA/CA-CZB-59X002/2020 (GenBank #MT394528), which was isolated from a patient in 2020 in Northern California and passaged once in Vero-E6 cells, was generously provided by Dr. Christopher Miller (University of California, Davis). To generate stocks for these studies, SARS-CoV-2 was passaged one additional time in Vero-E6 cells to achieve a titer of 2.2×10^7 plaque forming units (PFU)/mL. Single-use virus aliquots were stored at -80°C.

***N-dihydrogalactochitosan Treatment and SARS-CoV-2 Challenge*:** Sterile 1% weight/volume N-dihydrogalactochitosan (GC) was provided by Immunophotonics. GC was generated using Good Manufacturing Practices (GMP). Testing of GC included appearance, identity (1H NMR and UV/Vis), assay (HPLC), degree of galactation (1H NMR), viscosity, specific gravity, pH, microbiological (endotoxins and sterility), subvisible particulate matter, impurities (boron, galactose, galactitol, transition metals), molecular weight, and polydispersity indices. GC was presented as a 1.0% sterile solution (10 mg/ml) in 5 ml sealed vials and was diluted with sterile deionized water and sterile filtered 20X phosphate buffered saline (PBS) to a final concentration of 0.75% GC and 1X PBS. Mice were anesthetized with isoflurane and 40 µL of either diluted GC or PBS delivery vehicle was administered intranasally (i.n.) by a hanging drop over both nares. Mice were treated identically at 3 days and 1 day prior to challenge and 1 day post challenge. At challenge, mice were anesthetized and administered 30 µL of PBS or SARS-CoV-2 diluted in PBS at a dose of 10^3 or 10^4 PFU i.n. via hanging drop. Inocula were back-titrated to confirm the target dose. Mice were monitored twice daily for changes in weight, ruffled fur, ataxia, and labored breathing for up to 14 days. On days 1, 2 and 3, mice were anesthetized with isoflurane and throats were swabbed with rayon-tipped swabs (Puritan, Fisher Scientific, Fisher Scientific, Waltham, MA). Swabs were vortexed briefly in 400 µL of Dulbecco's Modified Eagles Medium (DMEM, Fisher Scientific, Waltham, MA) and frozen at -80°C. Mice were euthanized prior to experimental endpoint if weight loss exceeded 20% of the starting weight or if animals were deemed moribund as evidenced by limb weakness, ataxia or dragging of limbs, loss of limb function or rapid or depressed respiration rate. An adverse event was defined as any moribund disease signs at any time over the duration of the experiment. Prior to euthanasia, whole blood was collected by submandibular vein puncture under isoflurane anesthesia. Whole blood was clotted for >10 min at room temperature then centrifuged for 5 minutes at 8,000 x g and cleared serum was stored at -80°C. Mice were euthanized by isoflurane overdose and cervical dislocation then perfused with cold sterile PBS. Lung (right

inferior lobe) and brain (left hemisphere) were weighed and homogenized in 1-10 µL/mg DMEM with a sterile glass bead at 30 Hz for 4 minutes using a TissueLyser (Qiagen, Germantown, MD) automated homogenizer. Homogenates were cleared by centrifugation at 10,000 x g for 4 minutes and the cleared fraction was stored at -80°C.

***Histopathology*:** At necropsy, lungs were inflated with 10% buffered formalin (Fisher Scientific, Waltham, MA) and mice were fixed for 48 hours at room temperature in a 10-fold volume of 10% buffered formalin. Skulls were demineralized in a 10-fold volume of 0.5 M ethylenediamine tetraacetic acid (EDTA) (pH=7) at 4°C for 14 days, with EDTA solution exchanges every 3 days. Tissues were embedded in paraffin, thin-sectioned, and stained with hematoxylin and eosin (H&E). H&E-stained slides were scanned by a whole-slide image technique using an Aperio slide scanner (Leica, Buffalo Grove, IL) with a resolution of 0.24□µm/pixel. Image files were uploaded on a Leica hosted web-based site and a board certified veterinary anatomic pathologist without knowledge of treatment conditions evaluated sections for SARS-CoV-2 induced histologic lesions. For quantitative assessment of lung inflammation, digital images were captured and analyzed using ImageJ software (Fiji, NIH) to estimate the area of inflamed tissue that was visible to the naked eye at subgross magnification as a percentage of the total surface area of the lung section. Each lung section was scored as described (**Supplementary Table 1**).

***Plaque Assay*:** Washes from tracheal swabs, serum, residual inocula, and lung and brain homogenates were thawed and assayed. Samples were serially diluted 10-fold in DMEM with 1% bovine serum albumen (BSA) starting at an initial dilution of 1:8. 125 µL of each dilution was added to confluent Vero CCL-81 cells (ATCC, Manassas, VA) in 12-well plates with cell culture media decanted. Virus was incubated on cells for 1 hour at 5% CO2 in a humidified 37°C incubator. Cell monolayers were overlaid with 0.5% agarose dissolved in DMEM with 5% fetal bovine serum (FBS) and 1x antibiotic-antimycotic (Fisher Scientific, Waltham, MA) and incubated for 3 days at 5% CO2 and 37°C in a humidified incubator. Cells were fixed for >30

minutes with 4% formaldehyde then agarose plugs were removed. Cells were stained with 0.05% crystal violet in 20% ethanol for 10 minutes then rinsed three times with water. Plates were inverted to dry completely and the number of plaques in each well was counted. Viral titers were recorded as the reciprocal of the highest dilution where plaques were noted and are represented as PFU per swab or PFU per mg of solid tissue.

***Plaque Reduction Neutralization Test*:** Serum collected from mice at day 14 post inoculation was thawed at 37°C and 30 µL was heated in a water bath for 30 minutes at 56°C to inactivate complement proteins. Serum was diluted 4-fold with virus diluent consisting of PBS and 1% FBS, then samples were serially 2-fold diluted 11 times for a dynamic range of 1:4 to 1:4096. An equal volume of virus diluent containing 80 PFU of SARS-CoV-2 was added to each antibody dilution and a no-antibody control consisting of virus diluent only, resulting in a final dynamic range of 1:4 to 1:8192 with one no-antibody control. Antibody-virus dilution series were incubated for 1 hour at 37°C after which they were applied to confluent Vero CCL-81 cells in single-replicate and incubated for 1 hour at 5% CO2 and 37°C in a humidified incubator. Cells were overlaid, incubated, fixed, and stained as described above for plaque assays. Neutralizing titer is defined as the reciprocal of the dilution for which fewer than 20% of plaques were detected versus the no-antibody control (>80% neutralization).

***Statistics*:** All statistical tests were performed with GraphPad PRISM 9.0.2 (GraphPad Software). Logrank (Mantel-Cox) test for survival proportions were performed pairwise and *p*-values were adjusted with Bonferroni correction using R version 4.0.0 (R Project) p.adjust function. The correlation between mortality and positive virus detection was calculated by Fisher's exact test. Repeated measures two-way ANOVA tests were performed on log10-transformed viral titers and multiple comparisons were computed according to Tukey method. Main effect two-way ANOVA tests were performed on mouse weights normalized to starting values at the time of virus challenge or log10-transformed viral titers and multiple comparisons were computed with Tukey's method. Area under the curve (AUC) was calculated for

longitudinally collected tracheal swabs from days 1,2 and 3 and log10-transformed. ANOVA of grouped log10-AUC was performed with multiple comparisons computed with Tukey's method. ANOVA was performed on untransformed histologic scores or percentage of lung affected by inflammation and multiple comparisons were computed with Bonferroni's method. A Kruskal-Wallis H test was performed on untransformed PRNT80 neutralization values and multiple comparisons were computed according to Dunn's method.

DATA AVAILABILITY

All data contributing to the generation of figures and analyses described herein are available upon request from the corresponding author.

COMPETING INTERESTS

TH and SSKL declare a conflict of interest as employees with minority ownership stakes of Immunophotonics, Inc., the manufacturer of the proprietary immune stimulant GC. RML declares a conflict of interest as an advisor with minority ownership stake in Immunophotonics.

AUTHOR CONTRIBUTIONS

Conceptualization: RML, LLC, TH, SSKL, CMW, HL, and EEB. Investigation: CMW, HL, and EEB. Writing draft: CMW. Review and editing: CMW, HL, EEB, LLC, TH, SSKL,MKK, and RML. Visualization: CMW, EEB, MKK, LLC. Supervision and project administration: LLC. Funding acquisition: RML and LLC.

ACKNOWLEDGEMENTS

Funding support was provided by the UC Berkeley Henry Wheeler Center for Emerging and Neglected Diseases (CEND) COVID Catalyst Fund, and internal funding from the UC Davis

452 Office of the Vice Chancellor of Research. Funding sources did not influence experimental

453 design and analysis/interpretation of results or impact the decision to publish.

454

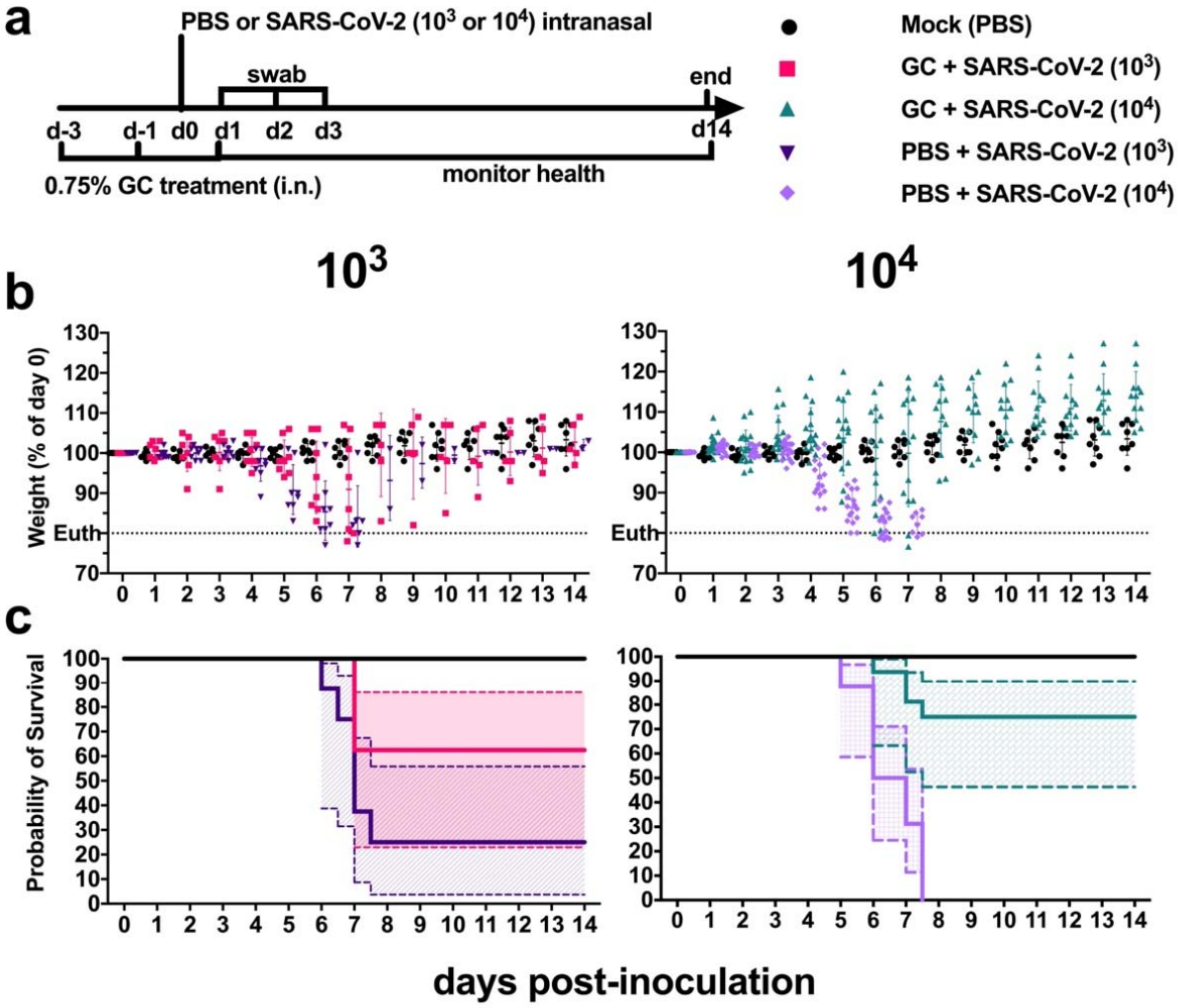

d **Survival comparisons**

GROUP 1	GROUP 2	P VALUE	SIGNIFICANCE
mock	GC + SARS-CoV-2 (10^3)	0.5024	ns
mock	GC + SARS-CoV-2 (10^4)	1.0000	ns
mock	SARS-CoV2 (10^3)	0.0200	*
mock	SARS-CoV-2 (10^4)	0.0001	****
GC + SARS-CoV-2 (10^3)	GC + SARS-CoV-2 (10^4)	1.0000	ns
GC + SARS-CoV-2 (10^3)	SARS-CoV2 (10^3)	0.0504	ns
GC + SARS-CoV-2 (10^4)	SARS-CoV-2 (10^4)	0.0001	****
SARS-CoV2 (10^3)	SARS-CoV-2 (10^4)	1.0000	ns

Fig. 1: N-dihydrogalactochitosan protects mice from SARS-CoV-2 mortality. (a) **Experimental design** where 6-week-old male and female hACE2 transgenic mice were treated with 0.75% GC or PBS delivery vehicle at days -3, -1 and +1 post-inoculation. Mice were challenged at day 0 with 10^3 or 10^4 PFU of SARS-CoV-2 or PBS (mock). Animals were weighed

daily, and throats were swabbed on days 1 through 3. (**b**) **Weight** represented as a percentage of individual mouse weight at the time of challenge. Euth = euthanasia cutoff. A main effect only model two-way ANOVA with Tukey corrected multiple comparisons yielded an F=52.80, p<0.0001, 4 degrees of freedom. Each symbol represents an individual mouse, and the horizontal lines show geometric mean and error bars are geometric standard deviation. **(c) Survival proportions.** The solid lines are survival proportions, and the shaded boxes show 95% confidence intervals. **(d) Logrank Mantel-Cox comparisons of survival proportions** with Bonferroni corrected p-values, multiple pairwise tests, 1 degree of freedom. n=8-16 per group, 2 combined experiments.

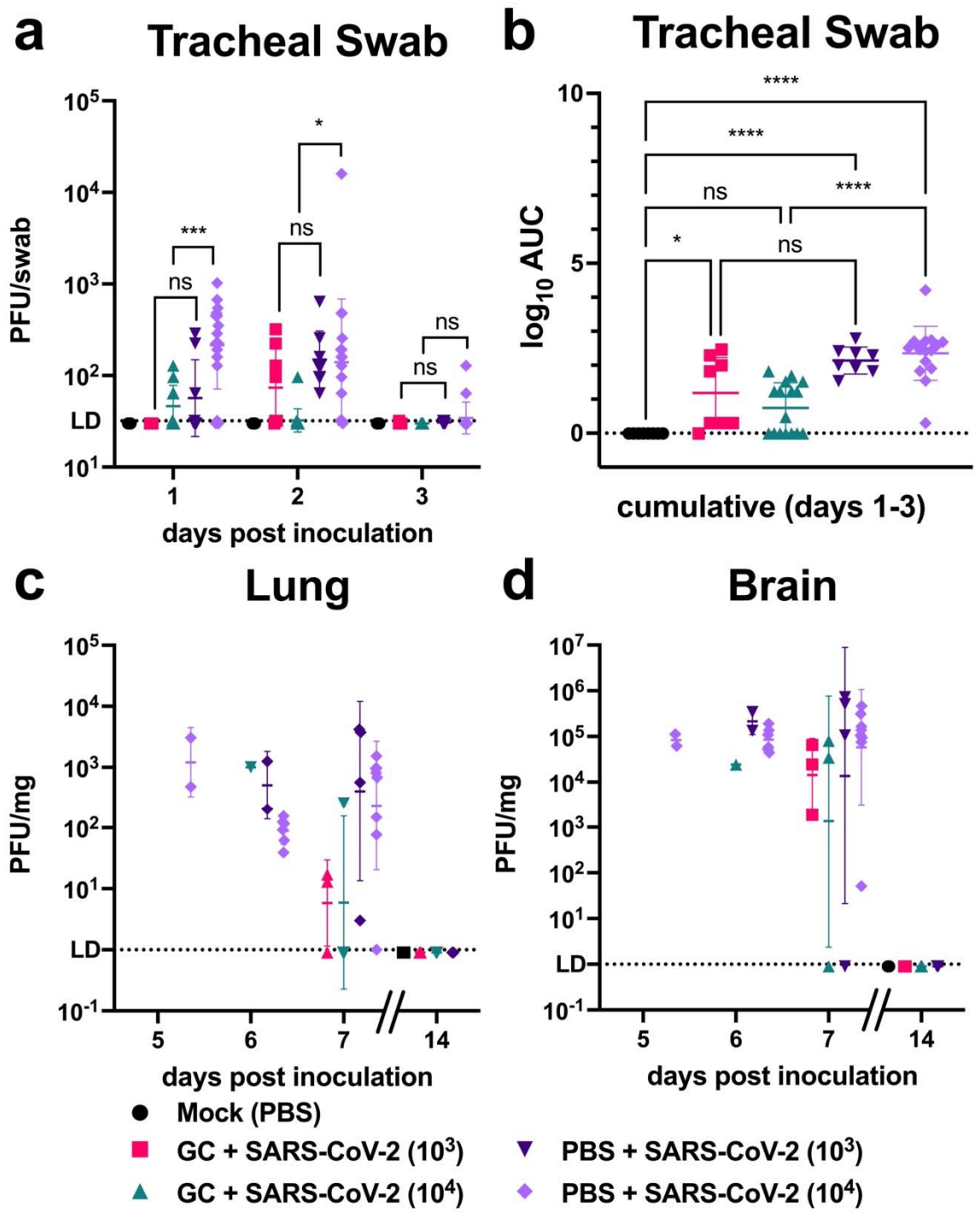

Fig. 2: N-dihydrogalactochitosan reduces SARS-CoV-2 detection in the upper respiratory tract. Infectious SARS-CoV-2 was measured in (**a**) **tracheal swabs** collected from hACE2 transgenic mice on days 1, 2 and 3 post inoculation. Repeated measures two-way ANOVA with Tukey corrected multiple comparisons on log10-transformed values, F=16.96, p<0.0001, 4

degrees of freedom. (**b) Total area under the curve** shows cumulative virus levels in swabs. ANOVA of log10-transformed total peak area with Tukey corrected multiple comparisons, F=7.538, p<0.0001, 4 degrees of freedom. Mice were necropsied on days 5, 6, 7 and 14 post-inoculation as euthanasia criteria were met. Infectious virus levels were measured in (**c**) **lung** and (**d**) **brain** at experimental endpoints. Main effects only model two-way ANOVA on log10-transformed values, F=2.431, p=0.0606, 4 degrees of freedom for lung, F=0.8134, p=0.5229, 4 degrees of freedom for brain. Symbols are individual animals, horizontal lines show geometric mean, and error bars represent geometric standard deviation. n=8-16 per group, 2 combined experiments. LD = limit of detection, AUC = area under the curve. * p < 0.05, *** p < 0.001, **** p < 0.0001.

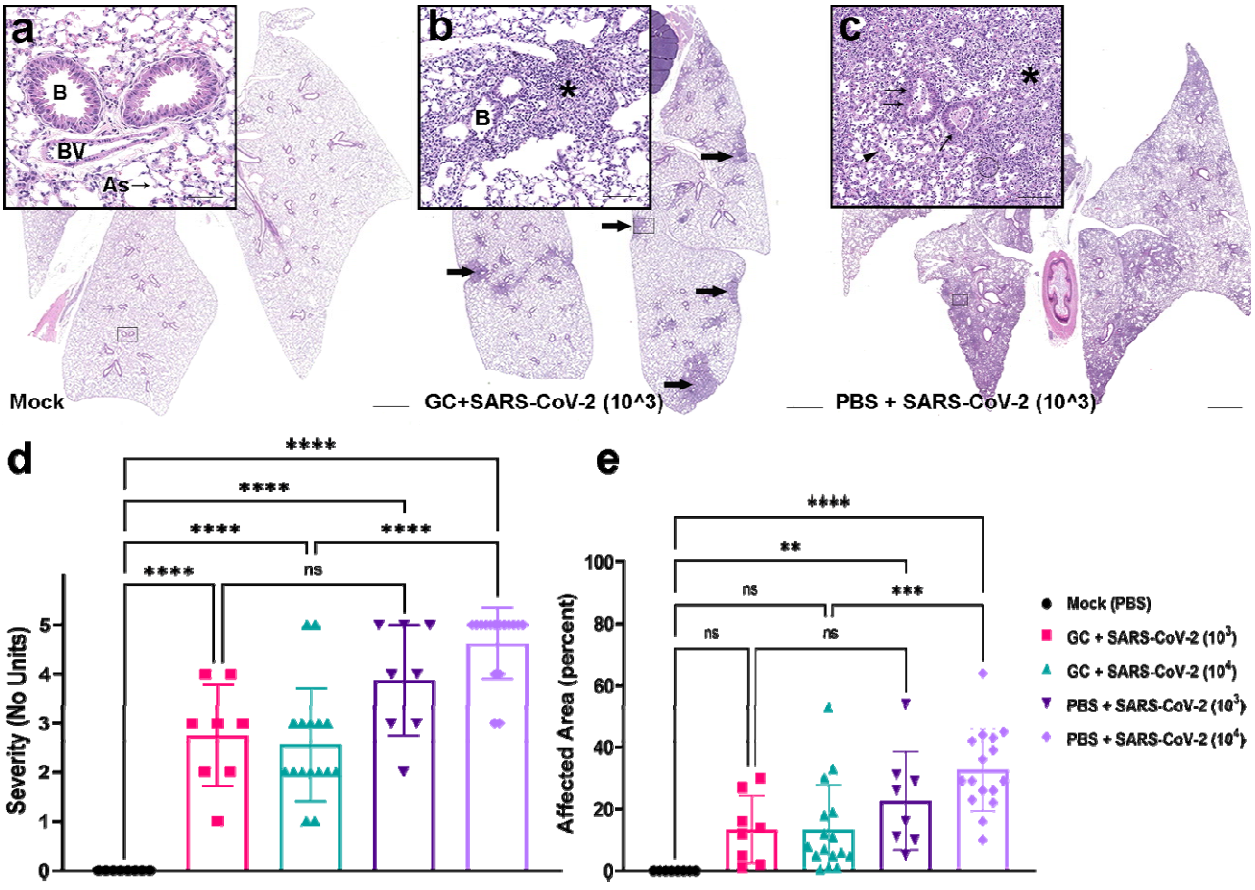

Fig. 3: N-dihydrogalactochitosan reduces histopathology associated with SARS-CoV-2 infection in lungs. Lungs from hACE2 transgenic mice were collected at the time of death, thin sectioned, and hematoxylin and eosin stained for histopathological scoring. Images show representative lungs. **(a) PBS-treated, mock inoculated mouse at day 14**, with normal bronchioles lined by epithelial cells, alveolar septa containing pulmonary capillaries lined by pneumocytes, and a small arteriole are visible in normal lung (inset). **(b) GC + 10^3 PFU SARS-CoV-2 mouse at day 7** with patchy inflammation (black arrows) distributed around airways and affecting approximately 15% of the section and peribronchiolar alveolar septal inflammation composed primarily of lymphocytes and macrophages with scattered multinucleated cells (inset). **(c) PBS + 10^3 PFU SARS-CoV-2 inoculated mouse at day 7** showing widespread, multifocal to coalescing inflammation affecting all lung lobes and approximately 60% of the section. Endotheliitis (circled) and bronchiolar epithelial hyperplasia characterized by

disorganization and piling-up of bronchiolar epithelium with increased mitotic figures (black arrows) is shown in inset. **(d) Lung lesion severity** was scored according to criteria defined in Supplementary Table 1 and the (**e**) **Total affected lung area** was estimated using image analysis software. Scale bars are 2 mm (subgross) and 50 µm (insets). As=alveolar septa, B=bronchioles, Br=bronchus, BV=blood vessel. ** $p < 0.01$, *** $p < 0.001$, **** $p < 0.0001$, ns=not significant. ANOVA, F=35.86, p<0.0001, 4 degrees of freedom (d). ANOVA, F=10.32, p<0.0001, 4 degrees of freedom (e). Symbols are individual animals, bars show the mean, and error bars show the standard deviation, n=8-16 per group, 2 combined experiments.

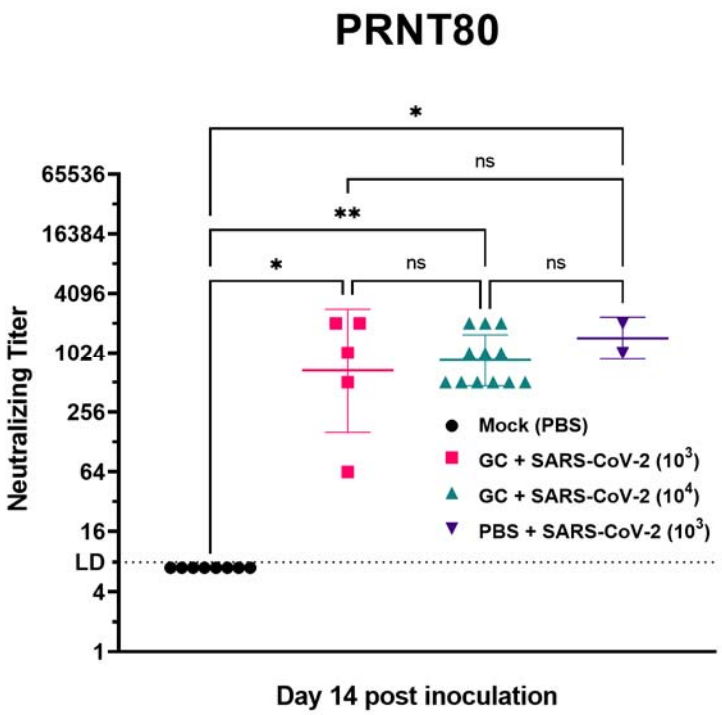

Fig. 4: N-dihydrogalactochitosan treated mice surviving SARS-CoV-2 challenge produce neutralizing antibodies. Neutralizing antibody was assessed by 80% plaque reduction neutralization test (PRNT80) in serum from hACE2 transgenic mice surviving to day 14 post inoculation. No PBS treated mice inoculated with 10^4 PFU SARS-CoV-2 were available for comparison due to uniform mortality. * $p < 0.05$, ** $p < 0.01$, LD = limit of detection. Kruskal-Wallis test with Dunn corrected multiple comparisons, H=17.87, p=0.0005, 3 degrees of freedom. Symbols are individual animals, horizontal lines are geometric mean and error bars show geometric standard deviation, n=2-12 per group, two combined experiments.

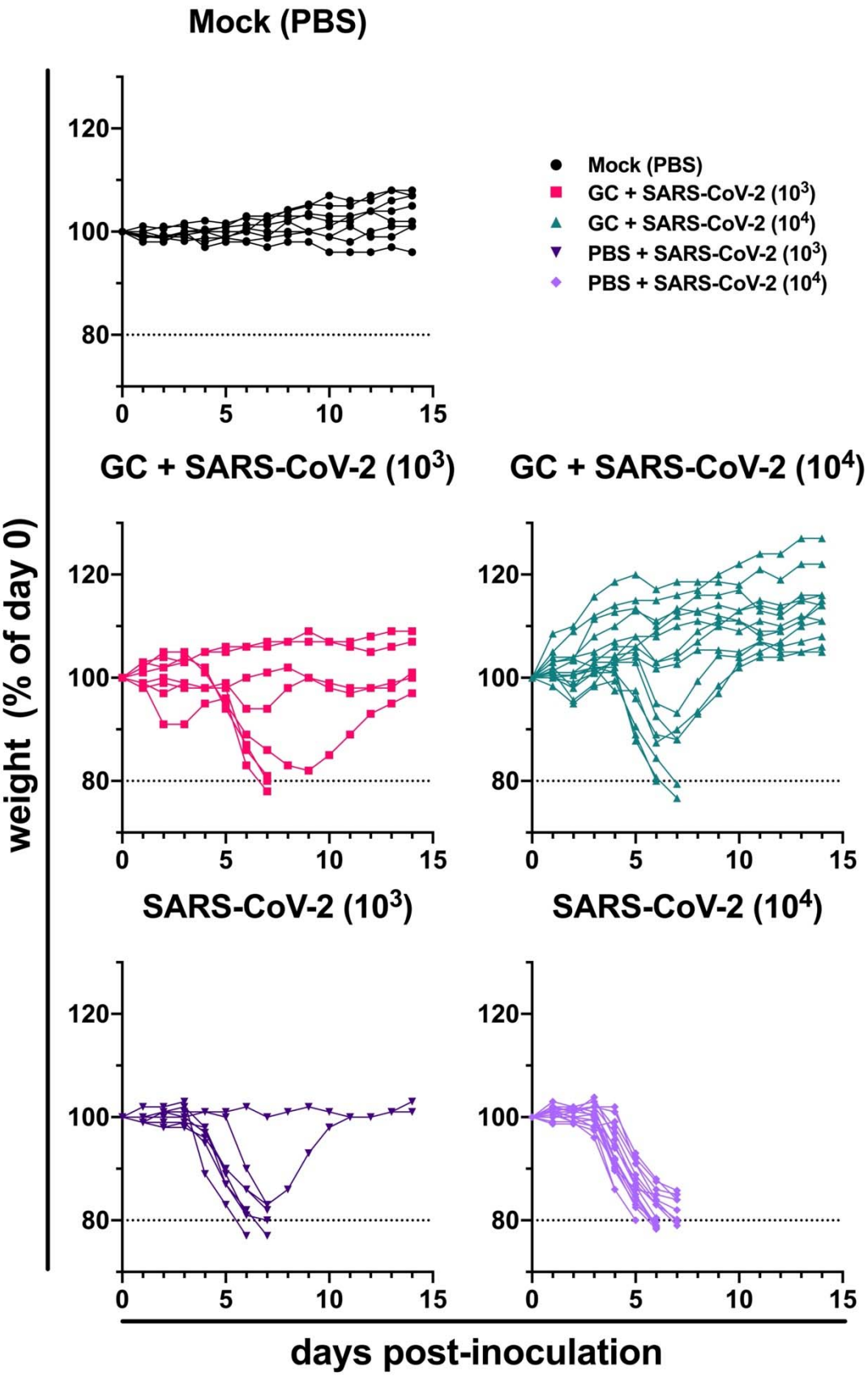

520

Supplementary Fig. 1: N-dihydrogalactochitosan protects mice from SARS-CoV-2 weight loss. Each line shows individual mouse weight as a percentage of their starting weight at the time of challenge.

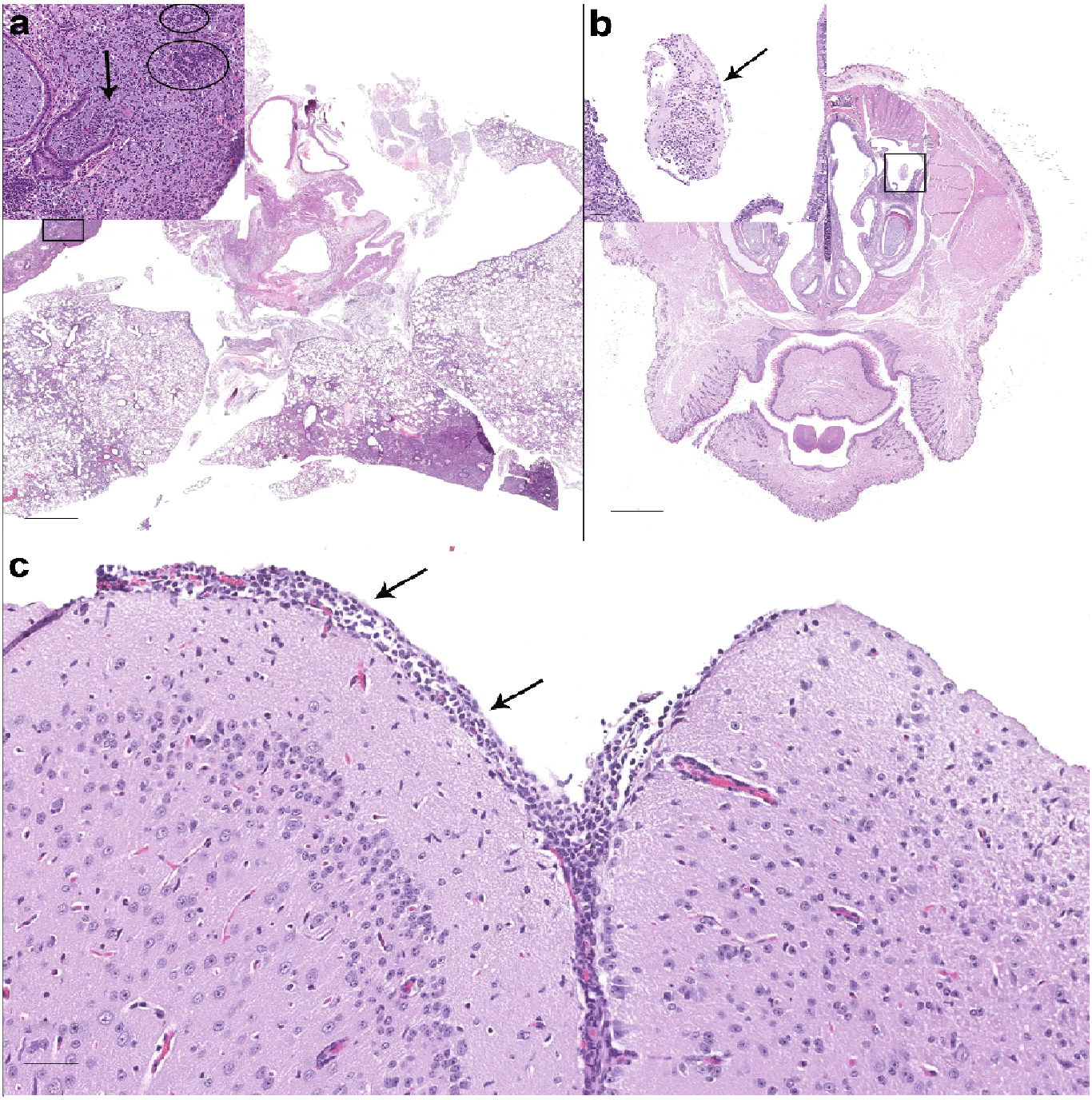

Supplementary Fig. 2: Additional photomicrographs of H&E-stained sections of lung, nasal cavity, and brain of hACE2 mice. **(a) Foreign material in lungs of some intranasally-treated animals.** Lung from a GC-treated 10^4 PFU SARS-CoV-2 inoculated male mouse at 7 days exhibits evidence of a foreign material reaction. Bronchioles are expanded by mucoid material, degenerate neutrophils and necrotic debris, with focal rupture of the bronchiolar wall (arrow),

extension of the inflammatory cells into adjacent alveoli, and foci of brightly eosinophilic foreign material surrounded by neutrophils and macrophages (circled) (inset). **(b-c) A subset of GC- or PBS-treated SARS-CoV-2 inoculated mice exhibit rhinitis and/or meningeal inflammation**. **(b)** Nasal cavity from a GC-treated 10^4 PFU SARS-CoV-2 inoculated female mouse at 6 days showing a focal exudate (box) composed of degenerate neutrophils and necrotic debris embedded in mucus (inset). **(c)** Brain from a GC-treated 10^3 PFU SARS-CoV-2 inoculated female mouse at 7 days with mild to moderate meningeal inflammation (arrows) composed primarily of lymphocytes with fewer macrophages. Scale bars are 1 mm (subgross) and 50 µm (insets). H&E stain.

Supplementary Table 1: Histopathology scoring criteria.

Score		Description
0	none	Within normal limits or rare, scattered lymphocytic infiltrates not observed in control animals but significance questionable (could be background lesion or variation of normal).
1	minimal	Minimal mononuclear inflammation affecting less than 2% of the section. Inflammatory leukocyte infiltration is limited to a perivascular and/or peribronchiolar distribution with no evidence of alveolar or vascular injury.
2	mild	Mild peribronchiolar/perivascular inflammation which may also expand alveoli/alveolar septa, composed primarily of macrophages and lymphocytes (+/- scattered neutrophils); increased alveolar macrophages; alveolar septal architecture largely intact; affects 2-10% of the section; and/or scattered alveolar hemorrhage/fibrin/edema; and/or scattered atypical/multinucleated syncytial cells.
3	moderate	Moderate bronchointerstitial and perivascular inflammation, increased alveolar macrophages, and/or alveolar hemorrhage/fibrin/edema (characterized as above); and/or alveolar damage (characterized by type I pneumocyte necrosis or loss with replacement by hyaline membranes, fibrin, edema, and/or necrotic debris); and/or reparative/regenerative changes (type II pneumocyte hyperplasia, atypical/multinucleated syncytial cells, or fibrosis); lesions affect 10-25% of the section.
4	severe	As above but more widespread inflammation, hemorrhage/fibrin/ edema, and/or alveolar damage/loss of normal septal architecture; and or regenerative changes affecting greater than 25% of the section.
+1		Add 1 point if: Greater than 25% of inflammatory cells are neutrophils; there is significant necrotizing vasculitis, endotheliitis or microthrombi; or if there is significant bronchiolitis, airway epithelial necrosis or hyperplasia.

REFERENCES

1. C. Huang, Y. Wang, X. Li, L. Ren, J. Zhao, Y. Hu, L. Zhang, G. Fan, J. Xu, X. Gu, Z. Cheng, T. Yu, J. Xia, Y. Wei, W. Wu, X. Xie, W. Yin, H. Li, M. Liu, Y. Xiao, H. Gao, L. Guo, J. Xie, G. Wang, R. Jiang, Z. Gao, Q. Jin, J. Wang, B. Cao, Clinical features of patients infected with 2019 novel coronavirus in Wuhan, China, *Lancet* (2020), doi:10.1016/S0140-6736(20)30183-5.

2. D. Wang, B. Hu, C. Hu, F. Zhu, X. Liu, J. Zhang, B. Wang, H. Xiang, Z. Cheng, Y. Xiong, Y. Zhao, Y. Li, X. Wang, Z. Peng, Clinical Characteristics of 138 Hospitalized Patients with 2019 Novel Coronavirus-Infected Pneumonia in Wuhan, China, *JAMA - J. Am. Med. Assoc.* **323**, 1061–1069 (2020).

3. N. Chen, M. Zhou, X. Dong, J. Qu, F. Gong, Y. Han, Y. Qiu, J. Wang, Y. Liu, Y. Wei, J. Xia, T. Yu, X. Zhang, L. Zhang, Epidemiological and clinical characteristics of 99 cases of 2019 novel coronavirus pneumonia in Wuhan, China: a descriptive study, *Lancet* **395**, 507–513 (2020).

4. F. Zhou, T. Yu, R. Du, G. Fan, Y. Liu, Z. Liu, J. Xiang, Y. Wang, B. Song, X. Gu, L. Guan, Y. Wei, H. Li, X. Wu, J. Xu, S. Tu, Y. Zhang, H. Chen, B. Cao, Clinical course and risk factors for mortality of adult inpatients with COVID-19 in Wuhan, China: a retrospective cohort study, *Lancet* **395**, 1054–1062 (2020).

5. J. Hellmuth, T. A. Barnett, B. M. Asken, J. D. Kelly, L. Torres, M. L. Stephens, B. Greenhouse, J. N. Martin, F. C. Chow, S. G. Deeks, M. Greene, B. L. Miller, W. Annan, T. J. Henrich, M. J. Peluso, Persistent COVID-19-associated neurocognitive symptoms in non-hospitalized patients, *J. Neurovirol.* **27**, 191–195 (2021).

6. E. L. Graham, J. R. Clark, Z. S. Orban, P. H. Lim, A. L. Szymanski, C. Taylor, R. M. DiBiase, D. T. Jia, R. Balabanov, S. U. Ho, A. Batra, E. M. Liotta, I. J. Koralnik, Persistent neurologic symptoms and cognitive dysfunction in non-hospitalized Covid-19 “long haulers,” *Ann. Clin. Transl. Neurol.* (2021), doi:10.1002/acn3.51350.

7. R. Lu, X. Zhao, J. Li, P. Niu, B. Yang, H. Wu, W. Wang, H. Song, B. Huang, N. Zhu, Y. Bi, X.

592 Ma, F. Zhan, L. Wang, T. Hu, H. Zhou, Z. Hu, W. Zhou, L. Zhao, J. Chen, Y. Meng, J. Wang, Y.
593 Lin, J. Yuan, Z. Xie, J. Ma, W. J. Liu, D. Wang, W. Xu, E. C. Holmes, G. F. Gao, G. Wu, W.
594 Chen, W. Shi, W. Tan, Genomic characterisation and epidemiology of 2019 novel coronavirus:
595 implications for virus origins and receptor binding, *Lancet* **395**, 565–574 (2020).
596 8. P. Zhou, X. Lou Yang, X. G. Wang, B. Hu, L. Zhang, W. Zhang, H. R. Si, Y. Zhu, B. Li, C. L.
597 Huang, H. D. Chen, J. Chen, Y. Luo, H. Guo, R. Di Jiang, M. Q. Liu, Y. Chen, X. R. Shen, X.
598 Wang, X. S. Zheng, K. Zhao, Q. J. Chen, F. Deng, L. L. Liu, B. Yan, F. X. Zhan, Y. Y. Wang, G.
599 F. Xiao, Z. L. Shi, A pneumonia outbreak associated with a new coronavirus of probable bat
600 origin, *Nature* **579**, 270–273 (2020).
601 9. S. S. Lakdawala, V. D. Menachery, The search for a COVID-19 animal model, *Science (80-.*
602 *).* **368**, 942–943 (2020).
603 10. C. Muñoz-Fontela, W. E. Dowling, S. G. P. Funnell, P. S. Gsell, A. X. Riveros-Balta, R. A.
604 Albrecht, H. Andersen, R. S. Baric, M. W. Carroll, M. Cavaleri, C. Qin, I. Crozier, K. Dallmeier, L.
605 de Waal, E. de Wit, L. Delang, E. Dohm, W. P. Duprex, D. Falzarano, C. L. Finch, M. B.
606 Frieman, B. S. Graham, L. E. Gralinski, K. Guilfoyle, B. L. Haagmans, G. A. Hamilton, A. L.
607 Hartman, S. Herfst, S. J. F. Kaptein, W. B. Klimstra, I. Knezevic, P. R. Krause, J. H. Kuhn, R. Le
608 Grand, M. G. Lewis, W. C. Liu, P. Maisonnasse, A. K. McElroy, V. Munster, N. Oreshkova, A. L.
609 Rasmussen, J. Rocha-Pereira, B. Rockx, E. Rodríguez, T. F. Rogers, F. J. Salguero, M.
610 Schotsaert, K. J. Stittelaar, H. J. Thibaut, C. Te Tseng, J. Vergara-Alert, M. Beer, T. Brasel, J. F.
611 W. Chan, A. García-Sastre, J. Neyts, S. Perlman, D. S. Reed, J. A. Richt, C. J. Roy, J. Segalés,
612 S. S. Vasan, A. M. Henao-Restrepo, D. H. Barouch, Animal models for COVID-19, *Nature* **586**,
613 509–515 (2020).
614 11. P. B. McCray, L. Pewe, C. Wohlford-Lenane, M. Hickey, L. Manzel, L. Shi, J. Netland, H. P.
615 Jia, C. Halabi, C. D. Sigmund, D. K. Meyerholz, P. Kirby, D. C. Look, S. Perlman, Lethal
616 Infection of K18-hACE2 Mice Infected with Severe Acute Respiratory Syndrome Coronavirus, *J.*
617 *Virol.* (2007), doi:10.1128/jvi.02012-06.

12. E. S. Winkler, A. L. Bailey, N. M. Kafai, S. Nair, B. T. McCune, J. Yu, J. M. Fox, R. E. Chen, J. T. Earnest, S. P. Keeler, J. H. Ritter, L. I. Kang, S. Dort, A. Robichaud, R. Head, M. J. Holtzman, M. S. Diamond, SARS-CoV-2 infection of human ACE2-transgenic mice causes severe lung inflammation and impaired function, *Nat. Immunol.* **21**, 1327–1335 (2020).

13. J. Zheng, L. Y. R. Wong, K. Li, A. K. Verma, M. E. Ortiz, C. Wohlford-Lenane, M. R. Leidinger, C. M. Knudson, D. K. Meyerholz, P. B. McCray, S. Perlman, COVID-19 treatments and pathogenesis including anosmia in K18-hACE2 mice, *Nature* **589**, 603–607 (2021).

14. Symptoms of COVID-19 | CDC (available at https://www.cdc.gov/coronavirus/2019-ncov/symptoms-testing/symptoms.html).

15. FDA Issues Emergency Use Authorization for Third COVID-19 Vaccine | FDA (available at https://www.fda.gov/news-events/press-announcements/fda-issues-emergency-use-authorization-third-covid-19-vaccine).

16. Coronavirus disease (COVID-19): Herd immunity, lockdowns and COVID-19 (available at https://www.who.int/news-room/q-a-detail/herd-immunity-lockdowns-and-covid-19).

17. A. Rhoades, *Veklury (remdesivir) EUA Letter of Approval, reissued 10/22/2020* (2020).

18. J. H. Beigel, K. M. Tomashek, L. E. Dodd, A. K. Mehta, B. S. Zingman, A. C. Kalil, E. Hohmann, H. Y. Chu, A. Luetkemeyer, S. Kline, D. Lopez de Castilla, R. W. Finberg, K. Dierberg, V. Tapson, L. Hsieh, T. F. Patterson, R. Paredes, D. A. Sweeney, W. R. Short, G. Touloumi, D. C. Lye, N. Ohmagari, M. Oh, G. M. Ruiz-Palacios, T. Benfield, G. Fätkenheuer, M. G. Kortepeter, R. L. Atmar, C. B. Creech, J. Lundgren, A. G. Babiker, S. Pett, J. D. Neaton, T. H. Burgess, T. Bonnett, M. Green, M. Makowski, A. Osinusi, S. Nayak, H. C. Lane, Remdesivir for the Treatment of Covid-19 — Final Report, *N. Engl. J. Med.* **383**, 1813–1826 (2020).

19. WHO recommends against the use of remdesivir in COVID-19 patients (available at https://www.who.int/news-room/feature-stories/detail/who-recommends-against-the-use-of-remdesivir-in-covid-19-patients).

20. Food and Drug Administration, *FDA Combating COVID-19 With Therapeutics* (2020)

644 (available at https://www.fda.gov/media/136832/download).

645 21. S. N. Chirkov, The antiviral activity of chitosan (review)*Appl. Biochem. Microbiol.* **38**, 1–8

646 (2002).

647 22. M. Mehrabi, H. Montazeri, M. N. Dounighi, A. Rashti, R. Vakili-Ghartavol, Chitosan-based

648 nanoparticles in mucosal vaccine delivery*Arch. Razi Inst.* **73**, 165–176 (2018).

649 23. X. Li, M. Min, N. Du, Y. Gu, T. Hode, M. Naylor, D. Chen, R. E. Nordquist, W. R. Chen,

650 Chitin, chitosan, and glycated chitosan regulate immune responses: The novel adjuvants for

651 cancer vaccine*Clin. Dev. Immunol.* **2013** (2013), doi:10.1155/2013/387023.

652 24. J. Mudgal, P. P. Mudgal, M. Kinra, R. Raval, Immunomodulatory role of chitosan-based

653 nanoparticles and oligosaccharides in cyclophosphamide-treated mice, *Scand. J. Immunol.* **89**,

654 e12749 (2019).

655 25. T. D. Carroll, S. Jegaskanda, S. R. Matzinger, L. Fritts, M. B. McChesney, S. J. Kent, J.

656 Fairman, C. J. Miller, A lipid/DNA adjuvant-inactivated influenza virus vaccine protects rhesus

657 macaques from uncontrolled virus replication afer heterosubtypic influenza a virus challenge, *J.*

658 *Infect. Dis.* (2018), doi:10.1093/infdis/jiy238.

659 26. X. Lei, X. Dong, R. Ma, W. Wang, X. Xiao, Z. Tian, C. Wang, Y. Wang, L. Li, L. Ren, F. Guo,

660 Z. Zhao, Z. Zhou, Z. Xiang, J. Wang, Activation and evasion of type I interferon responses by

661 SARS-CoV-2, *Nat. Commun.* **11** (2020), doi:10.1038/s41467-020-17665-9.

662 27. H. Xia, Z. Cao, X. Xie, X. Zhang, J. Y. C. Chen, H. Wang, V. D. Menachery, R. Rajsbaum,

663 P. Y. Shi, Evasion of Type I Interferon by SARS-CoV-2, *Cell Rep.* **33** (2020),

664 doi:10.1016/j.celrep.2020.108234.

665 28. M. S. Ribero, N. Jouvenet, M. Dreux, S. Nisole, Interplay between SARS-CoV-2 and the

666 type I interferon response*PLoS Pathog.* **16** (2020), doi:10.1371/journal.ppat.1008737.

667 29. M. Zheng, D. Qu, H. Wang, Z. Sun, X. Liu, J. Chen, C. Li, X. Li, Z. Chen, Intranasal

668 Administration of Chitosan Against Influenza A (H7N9) Virus Infection in a Mouse Model, *Sci.*

669 *Rep.* **6** (2016), doi:10.1038/srep28729.

30. X. Wang, W. Zhang, F. Liu, M. Zheng, D. Zheng, T. Zhang, Y. Yi, Y. Ding, J. Luo, C. Dai, H. Wang, B. Sun, Z. Chen, Intranasal immunization with live attenuated influenza vaccine plus chitosan as an adjuvant protects mice against homologous and heterologous virus challenge, *Arch. Virol.* **157**, 1451–1461 (2012).

31. B. Choi, D. H. Jo, A. K. M. M. Anower, S. M. S. Islam, S. Sohn, Chitosan as an Immunomodulating Adjuvant on T-Cells and Antigen-Presenting Cells in Herpes Simplex Virus Type 1 Infection, *Mediators Inflamm.* **2016** (2016), doi:10.1155/2016/4374375.

32. W. R. Chen, R. Carubelli, H. Liu, R. E. Nordquist, Laser immunotherapy: A novel treatment modality for metastatic tumors, *Appl. Biochem. Biotechnol. - Part B Mol. Biotechnol.* **25**, 37–43 (2003).

33. S. Song, F. Zhou, R. E. Nordquist, R. Carubelli, H. Liu, W. R. Chen, Glycated chitosan as a new non-toxic immunological stimulant Glycated chitosan immunological stimulant, *Immunopharmacol. Immunotoxicol.* **31**, 202–208 (2009).

34. I. Zizzari, C. Napoletano, F. Battisti, H. Rahimi, S. Caponnetto, L. Pierelli, M. Nuti, A. Rughetti, MGL Receptor and Immunity: When the Ligand Can Make the Difference, *J. Immunol. Res.* **2015** (2015), doi:10.1155/2015/450695.

35. M. Korbelik, J. Banáth, W. Zhang, T. Hode, S. Lam, P. Gallagher, J. Zhao, H. Zeng, W. Chen, N-dihydrogalactochitosan-supported tumor control by photothermal therapy and photothermal therapy-generated vaccine, *J. Photochem. Photobiol. B.* **204** (2020), doi:10.1016/J.JPHOTOBIOL.2020.111780.

36. M. Korbelik, T. Hode, S. S. K. Lam, W. R. Chen, Novel Immune Stimulant Amplifies Direct Tumoricidal Effect of Cancer Ablation Therapies and Their Systemic Antitumor Immune Efficacy*Cells* **10** (2021), doi:10.3390/cells10030492.

37. S. Qi, L. Lu, F. Zhou, Y. Chen, M. Xu, L. Chen, X. Yu, W. R. Chen, Z. Zhang, Neutrophil infiltration and whole-cell vaccine elicited by N-dihydrogalactochitosan combined with NIR phototherapy to enhance antitumor immune response and T cell immune memory, *Theranostics*

10, 1814–1832 (2020).

38. F. Zhou, J. Yang, Y. Zhang, M. Liu, M. L. Lang, M. Li, W. R. Chen, Local phototherapy synergizes with immunoadjuvant for treatment of pancreatic cancer through induced immunogenic tumor vaccine, *Clin. Cancer Res.* **24**, 5335–5346 (2018).

39. A. El-Hussein, S. S. K. Lam, J. Raker, W. R. Chen, M. R. Hamblin, N-dihydrogalactochitosan as a potent immune activator for dendritic cells, *J. Biomed. Mater. Res. - Part A* **105**, 963–972 (2017).

40. A. R. Hoover, K. Liu, C. I. Devette, J. R. Krawic, C. L. West, D. Medcalf, A. L. Welm, X.-H. Sun, W. H. Hildebrand, W. R. Chen, ScRNA-seq reveals tumor microenvironment remodeling induced by local intervention-based immunotherapy, *bioRxiv* , 2020.10.02.323006 (2020).

41. C. Brown, J. Vostok, H. Johnson, M. Burns, R. Gharpure, S. Sami, R. Sabo, N. Hall, A. Foreman, P. Schubert, G. Gallagher, T. Fink, L. Madoff, S. Gabriel, B. MacInnis, D. Park, K. Siddle, V. Harik, D. Arvidson, T. Brock-Fisher, M. Dunn, A. Kearns, A. Laney, Outbreak of SARS-CoV-2 Infections, Including COVID-19 Vaccine Breakthrough Infections, Associated with Large Public Gatherings - Barnstable County, Massachusetts, July 2021, *MMWR. Morb. Mortal. Wkly. Rep.* **70**, 1059–1062 (2021).

42. B. Bellich, I. D'Agostino, S. Semeraro, A. Gamini, A. Cesàro, "The Good, the Bad and the Ugly" of Chitosans, *Mar. Drugs* **14** (2016), doi:10.3390/MD14050099.

43. K. Jayathilakan, K. Sultana, K. Radhakrishna, A. S. Bawa, Utilization of byproducts and waste materials from meat, poultry and fish processing industries: A review*J. Food Sci. Technol.* **49**, 278–293 (2012).

44. N. A. Negm, H. H. H. Hefni, A. A. A. Abd-Elaal, E. A. Badr, M. T. H. Abou Kana, Advancement on modification of chitosan biopolymer and its potential applications*Int. J. Biol. Macromol.* **152**, 681–702 (2020).

45. H. Mokhtar, L. Biffar, S. Somavarapu, J. P. Frossard, S. McGowan, M. Pedrera, R. Strong, J. C. Edwards, M. Garcia-Durán, M. J. Rodriguez, G. R. Stewart, F. Steinbach, S. P. Graham,

722 Evaluation of hydrophobic chitosan-based particulate formulations of porcine reproductive and
723 respiratory syndrome virus vaccine candidate T cell antigens, *Vet. Microbiol.* **209**, 66–74 (2017).
724 46. S. Shim, H. E. Park, S. H. Soh, Y. Bin Im, H. S. Yoo, Induction of Th2 response through
725 TLR2-mediated MyD88-dependent pathway in human microfold cells stimulated with chitosan
726 nanoparticles loaded with Brucella abortus Mdh, *Microb. Pathog.* **142** (2020),
727 doi:10.1016/j.micpath.2020.104040.
728 47. X. Zhang, K. Wu, D. Wang, X. Yue, D. Song, Y. Zhu, J. Wu, Nucleocapsid protein of SARS-
729 CoV activates interleukin-6 expression through cellular transcription factor NF-κB, *Virology* **365**,
730 324–335 (2007).
731 48. D. Blanco-Melo, B. E. Nilsson-Payant, W. C. Liu, S. Uhl, D. Hoagland, R. Møller, T. X.
732 Jordan, K. Oishi, M. Panis, D. Sachs, T. T. Wang, R. E. Schwartz, J. K. Lim, R. A. Albrecht, B.
733 R. tenOever, Imbalanced Host Response to SARS-CoV-2 Drives Development of COVID-19,
734 *Cell* **181**, 1036-1045.e9 (2020).
735 49. C. Pyle, F. Uwadiae, D. Swieboda, J. Harker, Early IL-6 signalling promotes IL-27
736 dependent maturation of regulatory T cells in the lungs and resolution of viral immunopathology,
737 *PLoS Pathog.* **13** (2017), doi:10.1371/JOURNAL.PPAT.1006640.
738 50. C. L. Bueter, C. K. Lee, V. A. K. Rathinam, G. J. Healy, C. H. Taron, C. A. Specht, S. M.
739 Levitz, Chitosan but not chitin activates the inflammasome by a mechanism dependent upon
740 phagocytosis, *J. Biol. Chem.* **286**, 35447–35455 (2011).
741 51. E. C. Carroll, L. Jin, A. Mori, N. Muñoz-Wolf, E. Oleszycka, H. B. T. Moran, S. Mansouri, C.
742 P. McEntee, E. Lambe, E. M. Agger, P. Andersen, C. Cunningham, P. Hertzog, K. A. Fitzgerald,
743 A. G. Bowie, E. C. Lavelle, The Vaccine Adjuvant Chitosan Promotes Cellular Immunity via DNA
744 Sensor cGAS-STING-Dependent Induction of Type I Interferons, *Immunity* **44**, 597–608 (2016).
745 52. B. Sun, S. Yu, D. Zhao, S. Guo, X. Wang, K. Zhao, Polysaccharides as vaccine
746 adjuvants*Vaccine* **36**, 5226–5234 (2018).
747 53. R. C. Read, S. C. Naylor, C. W. Potter, J. Bond, I. Jabbal-Gill, A. Fisher, L. Illum, R.

748 Jennings, Effective nasal influenza vaccine delivery using chitosan, *Vaccine* **23**, 4367–4374
749 (2005).
750 54. D. Elieh Ali Komi, L. Sharma, C. S. Dela Cruz, Chitin and Its Effects on Inflammatory and
751 Immune Responses*Clin. Rev. Allergy Immunol.* **54**, 213–223 (2018).
752 55. S. Bashiri, P. Koirala, I. Toth, M. Skwarczynski, Carbohydrate immune adjuvants in subunit
753 vaccines*Pharmaceutics* **12**, 1–33 (2020).
754 56. C. L. Bueter, C. A. Specht, S. M. Levitz, Innate Sensing of Chitin and Chitosan, *PLoS*
755 *Pathog.* **9** (2013), doi:10.1371/journal.ppat.1003080.
756 57. J. Seetharaman, A. Kfanigsberg, R. Slaaby, H. Leffler, S. H. Barondes, J. M. Rini, X-ray
757 crystal structure of the human galectin-3 carbohydrate recognition domain at 2.1-Å resolution, *J.*
758 *Biol. Chem.* **273**, 13047–13052 (1998).
759 58. T. Semeňuk, P. Krist, J. Pavlíček, K. Bezouška, M. Kuzma, P. Novák, V. Křen, Synthesis of
760 chitooligomer-based glycoconjugates and their binding to the rat natural killer cell activation
761 receptor NKR-P1, *Glycoconj. J.* **18**, 817–826 (2001).
762 59. F. Zhou, S. Wu, S. Song, W. R. Chen, D. E. Resasco, D. Xing, Antitumor immunologically
763 modified carbon nanotubes for photothermal therapy, *Biomaterials* **33**, 3235–3242 (2012).
764 60. R. J. Nevagi, Z. G. Khalil, W. M. Hussein, J. Powell, M. R. Batzloff, R. J. Capon, M. F. Good,
765 M. Skwarczynski, I. Toth, Polyglutamic acid-trimethyl chitosan-based intranasal peptide nano-
766 vaccine induces potent immune responses against group A streptococcus, *Acta Biomater.* **80**,
767 278–287 (2018).
768 61. F. Micoli, P. Costantino, R. Adamo, Potential targets for next generation antimicrobial
769 glycoconjugate vaccines*FEMS Microbiol. Rev.* **42**, 388–423 (2018).
770